

## RESEARCH ARTICLE

 OPEN ACCESS

Received: 17-10-2023

Accepted: 23-10-2023

Published: 20-12-2023

**Citation:** Devaraj LD, Srinivasan V (2023) Evaluation of Micro Hardness and Wear Characteristics of Gyroid Designed Ti-6Al-4V Fabricated Through DMLS Technique. Indian Journal of Science and Technology 16(47): 4469-4480. <https://doi.org/10.17485/IJST/v16i47.2637>

\* **Corresponding author.**[danieldevament96@gmail.com](mailto:danieldevament96@gmail.com)**Funding:** None**Competing Interests:** None

**Copyright:** © 2023 Devaraj & Srinivasan. This is an open access article distributed under the terms of the [Creative Commons Attribution License](https://creativecommons.org/licenses/by/4.0/), which permits unrestricted use, distribution, and reproduction in any medium, provided the original author and source are credited.

Published By Indian Society for Education and Environment ([iSee](https://www.indjst.org/))

**ISSN**

Print: 0974-6846

Electronic: 0974-5645

# Evaluation of Micro Hardness and Wear Characteristics of Gyroid Designed Ti-6Al-4V Fabricated Through DMLS Technique

L Daniel Devaraj<sup>1\*</sup>, V Srinivasan<sup>2</sup>

<sup>1</sup> Reseach Scholar, Department of Manufacturing Engineering, Faculty of Engineering and Technology, Annamalai University, Annamalai Nagar, 608 002, Tamil Nadu, India

<sup>2</sup> Associate Professor, Department of Manufacturing Engineering, Faculty of Engineering and Technology, Annamalai University, Annamalai Nagar, 608 002, Tamil Nadu, India

## Abstract

**Objectives:** To investigate the Micro Hardness, Micro structures and wear characteristics of the TPMS (Triply Periodic Minimal Surface) Gyroid structures with optimized porosity percentage for Bio medical application. **Methods:** Micro Hardness tester is used to find the micro hardness of the as cast Ti-6Al-4V and Gyroid Ti-6Al-4V Sample. Wear tests using pin-on-disc tribometer was used to assess the Gyroid Ti-6Al-4V wear samples for various loads and sliding velocity. The wear test parameters were test as load of 10, 30 & 50 N, with the sliding velocity of 0.5, 1.0 7 1.5 m/s. Atomic force microscope has been used for finding the surface roughness of the as cast and Gyroid Ti-6Al-4V samples before and after wear test. **Findings:** According to the test results. It is found that Gyroid Ti-6Al-4V samples posses more wear resistance than as cast Ti-6Al-4V. The micro hardness test results depicted clearly that, the Gyroid Ti-6Al-4V alloy posses' micro hardness of 408 HV in comparison with as cast Ti-6Al-4V alloys' hardness of 358 HV. The morphological characteristics of the worn-out samples were investigated using scanning electron microscope. At higher sliding conditions occurrence of large friction events lead to higher wear rates and the periodic localised fracture of transfer layer. At low sliding conditions, the Gyroid Ti-6Al-4V samples experienced ploughing, peeling off, plastic deformation types of wear mechanism. **Novelty:** The wear modes were categorised by the Fuzzy C-means algorithm, and a novel PNN tool in MATLAB created a wear map mechanism suitable for the Gyroid Ti alloy. The research conducted in this paper demonstrates a novel methodology for investigating wear mapping using a Probabilistic Neural Network on wear samples with a Gyroid lattice structure.

**Keywords:** TPMS; Lattice/porous structure; Micro Hardness; Wear Characteristics; Ti-6Al-4V

## 1 Introduction

Due to the need for complicated and varied parts in real life, 3D printing is now a growing industry in the manufacturing sector. The method of combining materials that are identical to create a component from a 3D CAD model is known as additive manufacturing, often known as 3D printing. This process is typically carried out layer by layer as opposed to subtractive manufacturing<sup>(1)</sup>. The extra costs associated with producing a product have been significantly reduced by the usage of 3D printing. However, recently a variety of industries are embracing 3D printing, from designs to finished goods. Owing to the expenses associated with production items that are specifically designed for end consumers, product customization has proven difficult for manufacturers. In contrast, AM can 3D print customised goods in moderate size at an affordable price. This is especially helpful in the biomedical applications, where exclusive patient-specific devices are frequently needed<sup>(2)</sup>.

Typically, biological architectures are very porous, which is characterised as having a large volume proportion of pores in solid materials. They both weigh considerably less than the solid in the same volume. There has been invention of natural cellular architectures that combine the benefits of low density, higher specific strength, and multi functionality. In the past majority of metallic implants were produced using older methods such as forging, hot rolling, investment casting, and machining. But in recent years, a new technique known as additive manufacturing (AM) has used<sup>(3)</sup>. The prevention of the "stress shielding" phenomenon is the main advantage of diminishing the elastic modulus of the titanium alloy used in orthopaedic implants. This effect is linked to the fact that the rigid metal placed next to the bone will support the majority of the weight, putting less strain on the bones. Since porous metals have greater osseointegration, the artificial porosity also improves the metallic substance from a biological standpoint<sup>(4)</sup>.

In a wide range of industrial applications, including the aircraft industry, biomedical, and power/energy sectors, titanium (Ti) and its alloys, particularly the most widely used Ti-6Al-4V alloys is emerged as one of the most significant high-end materials. This is connected to its superior corrosion resistance, the highest specific strength of all metals, and low density. Additionally, the material has strong specific strength at high temperatures<sup>(5)</sup>. A metallic material's microstructure can change significantly depending on the production processes used, which can lead to highly diverse mechanical and physical characteristics as well as unique wear resistance. Above the transus temperature, which is normally above 950 °C, the Ti6Al4V alloy is organised in a  $\beta$  phase, and below this temperature Ti alloys are organized in a  $\alpha + \beta$  phase<sup>(6)</sup>.

Ti-6Al-4V is mainly utilized for Prosthetic implants (such as shoulder and elbow replacements), orthopaedic and dental implant devices, tissue engineering, cardiac simulators, and stents are other prominent uses. It is either employed for replacing or supporting physiological pursuit to enhance human life quality by healing illnesses and repairing damaged body components. The alloy still has to have its tribological and fatigue properties improved in order to be more suitable for use as a load-bearing bio-implant. One of the main reasons for implant failure is the implant's poor interface integration with natural bone<sup>(7)</sup>. In survey, numerous research teams examined the wear characteristics of Ti-6Al-4V alloy by a pin-on-disk test. The wear factor for load-bearing synovial joints like the hip and knee is around 106 mm<sup>3</sup>/N, while the typical coefficient of friction is around 0.02. However, depending on the materials in contact the type of lubricant utilised for testing, the friction coefficient for implant materials ranges from 0.16 to 0.05. In comparison to metal on polyethylene bearings, metal on metal prosthesis is shown to yield 20–100 times reduced wear volumes<sup>(8)</sup>. To improve the performance with regard to wear behaviour, it is necessary to have a strong understanding of the friction and wear processes of titanium and its alloys. The wear properties of bio implants by titanium alloys in simulated bodily fluid must also be properly assessed<sup>(9)</sup>. Nevertheless, they are frequently utilised for initial material evaluation and characterisation of wear behaviour and are helpful for forecasting the wear performance and behaviour of the materials in vivo<sup>(10)</sup>. Abrasive and adhesion wear are the general categories used to describe the mechanism of wear for titanium and its alloys. Adhesive wear is a primary wear process in a live organism since biomedical implants like titanium alloy offers low wear in a bodily fluid than in environment.

The work's objective is to investigate comparative wear characteristics of DMLS'ed Gyroid Ti-6Al-4V and as cast Ti-6Al-4V alloy that are suitable for biomedical application. Additionally, it is necessary to assess the influence of process variables such as normal load, sliding velocity and sliding distance on the wear characteristics of Ti alloy on pin on disc tester under lubricated condition. Further, in order to study the sustainability of Gyroid Ti alloy. Microhardness, XRD and SEM analysis are implied in this investigation.

## 2 Methodology

### 2.1 Materials

The powder's chemical make-up is in accordance with ASTM F3001 for the EOS Ti Grade 23 alloy. The Ti alloy powder, with a size of around 40 $\mu$ , was supplied by EOS, Germany. The 3D printing of Ti-6Al-4V samples were fabricated at CTTC,

Bhubaneswar in accordance with ASTM B348 standard using Laser Powder Bed Fusion - Technology by DMLS EOS M280 machine. The chemical composition of Ti-6Al-4V is shown in Table 1.

**Table 1. Chemical constitution of Ti-6Al-4V Grade 23**

Element	Ti	Al	V	O	N	C	H	Fe	Y
Percentage	87.973	6.5	4.5	0.13	0.05	0.08	0.012	0.25	0.005

### 2.1.1 Process Parameters

A high-power laser beam of 340W was focused on a powder bed consisting of Ti-6Al-4V powder, where the powder undergoes solidification after local heating. As a consequence, the building of physical 3D geometries according to the AM shaping principle in compliance with ASTM 59200 - 2021 was achieved by adding material to each layer. Optimized process variables, such as laser power, hatch distance, scan velocity, and layer thickness, were chosen and used for this investigation based on the literature and the OEM of the machine<sup>(11)</sup>.

## 2.2 Physical and Mechanical Characterization

### 2.2.1 Optical Microscope

The Kroll's reagent, which comprises 100 ml, 2-6 ml HnO<sub>3</sub>, 1-3 ml Hcl of water, was employed to polish the specimens of Gyroid Ti-6Al-4V. The Olympus BX53M optical microscope in MatricsTech, Nagercoil was used to capture the microstructures at various magnifications in accordance with ASTM F410. The micro structural analysis embraced grain limits, the specimens' grain size, Interfacial area in relation to volume size of the component phase stages' number and dispersion.

### 2.2.2 Scanning Electron Microscope (SEM)

After the wear test, the surface morphology of the printed samples was examined using CAREL ZEISS EVO-18 scanning electron microscope. Facilitated by St. Joseph's College, Trichy. The samples were cut using a CNC wire cut EDM to a size of 10x10x6mm for determining various wear mechanisms such as abrasion, oxidation, delamination, and melting.

### 2.2.3 Atomic Force Microscope

The topographical information's like average roughness value and the maximum mean peak height were assessed using AFM (AGILENT -5500) fabricated by CISL, Annamalai University. The AFM samples were cut using a CNC wire cut EDM to a size of 10x10x6mm. The AFM produced both 2D and 3D images, where the vertical deviations of the 3D pictures were used to assess the surface roughness.

### 2.2.4 X-Ray diffraction analysis (XRD)

The crystalline structure and orientation of the material were determined using an X-ray diffractometer. This experiment was carried out in an X' pert powder XRD facilitated by department of chemistry, Annamalai University. In the difference pattern, a single crystal only generates one set of peaks. By employing an X-ray diffractometer (XRD) and a Malvern Panalytical with a Cu K  $\alpha$  2 $\theta$  gradient of 0 -150 °, the phase compositions of the materials were determined.

### 2.2.5 Vicker's Micro Hardness

By using an automated Vickers hardness measurement instrument (shimatzu S200), the hardness of the additively printed Ti-6Al-4V lattice sample was determined. The load and dwell time were chosen to be 1000g and 10 s, respectively, to ensure the homogeneity of hardness evaluation. Both Gyroid Ti-6Al-4V and as cast Ti samples were subjected to indentation and the average values of micro hardness was drawn from total of five readings.

### 2.2.6 Pin on Disc Wear Test

The wear tests were conducted with the help of pin-on-disc tribometer (Novus Tribo solutions) in Metro Composites, Chennai. According to ASTM G99, the samples were fabricated for the height of 20 mm, with the diameter of 10 mm. Three process parameters load, velocity and sliding distance were selected to conduct the wear test in the wet condition. The Simulated Body Fluid is used as the lubrication for the wear test which is supplied by the drop-by-drop action by a controlled motor. The computer was synced with the pin on disc device to display the results pertaining to wear studies.

### 3 Results and discussion

#### 3.1 Physical and Mechanical Evaluation

##### 3.1.1 Microstructural analysis

The optical micrograph shown in Figure 1 depicts the morphology of the Gyroid Ti-6Al-4V alloy. The columnar grains were filled with extremely thin, orthogonally adjusted martensitic laths emanating from the columnar grain boundaries<sup>(12)</sup>. The fine martensitic laths are metastable in nature, and the columnar grain subsequent boundaries are the previous grains formed during solidification. The microstructure of the Ti6Al4V alloy developed using the process of additive manufacturing demonstrated the presence of a refined equiaxed grain structure, characterised by a consistent dispersion of both  $\alpha$  and  $\beta$  phases throughout the material<sup>(13)</sup>. The rate of cooling is the main factor in microstructure development. At a temperature of around 875°C,  $\beta$ -phase often converts to  $\alpha$ -phase in the processing of Ti-6Al-4V when the cooling rate is modest. However, Gyroid Ti-6Al-4V sample when subjected to cooling speeds more than 525 K/s are completely martensitic. Some studies have proved that the tensile strength, average elongation, and Vickers hardness were boosted by utilising the facet clustering model and in AM approach, While the surface roughness was reduced during the above process<sup>(14)</sup>. While there were no obvious characteristics in the  $\alpha'$  martensitic phase, the 3D printed Ti6Al4V alloy was dominated by  $\alpha'$  martensitic majority microstructure.

Further it is observed from the above study that the vertically built specimens were characterised by martensite needles, while the horizontally built specimens characterised by acicular structure<sup>(15)</sup>.

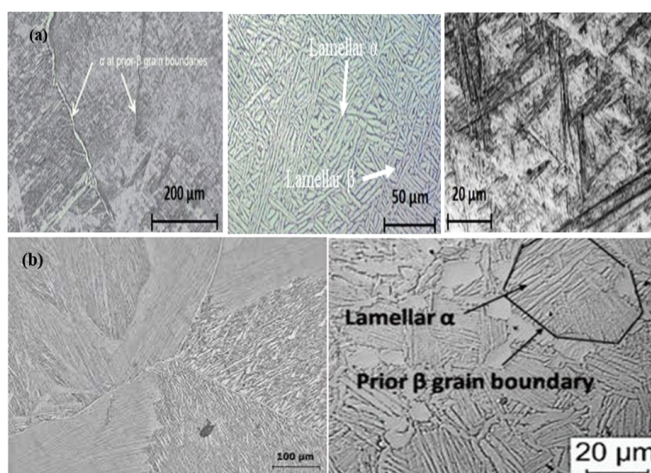


Fig 1. a) Microstructure of Gyroid Ti-6Al-4V sample b) Microstructure of as cast Ti-6Al-4V

At elevated temperature rise, Ti-6Al-4V exhibit one or two crystal structures alpha phase ( $\alpha$ ), a HCP structure often present at ambient temperature, the beta phase ( $\beta$ ), a BCC structure stable at high temperatures. Grain nucleation and growth begin when the liquid Ti alloys initiates solidification. Vanadium functions as a stabiliser element in Ti6Al4V alloys, enabling the presence of a small stable percentage of the  $\beta$  phase at ambient temperature. Because of this, the Ti6Al4V alloy exhibits a combination of ( $\alpha + \beta$ ) phases at normal room temperature. The white coloured lamellar ( $\alpha$ ) structure and black coloured lamellar ( $\beta$ ) structure is shown in Figure 1(a). Depending on the heat cycles undergone, these phases can display a wide range of microstructures and characteristics<sup>(16)</sup>.

Figure 1(b) shows the micro structural images of as cast Ti alloys, which is dominated by lamellar and altered phases of  $\alpha$  and  $\beta$  Ti-6Al-4V alloys. The Widmannstetter structural features are visible in the microstructure of the untreated specimen at 980 °C, which is above the transus temperature. The smaller the equiaxial percentage and the greater the lamellar thickness, the higher will be solid solution treatment temperature. These are in lined with the studies of Gong et. Al. The Ti6Al4V alloys are well known for having a "  $\alpha$  phase" (hcp) at low temperatures that can change into a "  $\beta$  phase" (bcc) at higher temperatures<sup>(17)</sup>.

##### 3.1.2 Microhardness

Figure 2 displays the micro hardness results of both as cast and Gyroid Ti alloys. The micro hardness of as cast Ti alloy is clocked to 358 HV, while the Gyroid Ti alloy acquired Micro hardness of 460 HV. In comparison with as cast Ti alloy the hardness of the Gyroid Ti-6Al-4V arose by 22.18 %. Owing to rapid cooling rate during liquid and solidus temperatures, a significant solid-

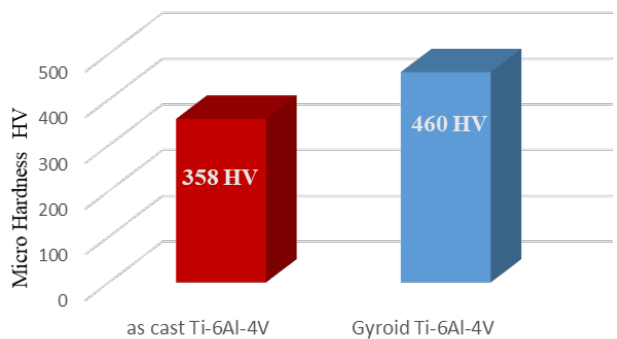


Fig 2. Microhardness of Casted and Printed Ti-6Al-4V

state phase changes occur<sup>(18)</sup>. As a result, the produced samples frequently do not have enough time to achieve equilibrium microstructures. In other words, some phase transitions are resulted by the frequently constrained quick heat cycles. This study infers that a desired hardness may be achieved through Additive Manufacturing Technique. Even though, residual porosity present in the DMLSed Ti-6Al-4V alloy is detrimental to the metallurgical characteristics, the micro hardness of the samples was significantly enhanced due to the influence of cooling rate and molten pool shape. The micro hardness value of (460 HV) observed in this study is greater than the micro hardness values of (409 HV) by Thijs et.al<sup>(19)</sup>. Due to variations in hatch spacing, that eventually influence cooling rates and the ensuing microstructure, the micro hardness of Gyroid Ti alloy is greater than that of as cast Ti alloy. The enhanced micro hardness of the additively produced Gyroid Ti-6Al-4V can be attributed to the alterations in its microstructure, including variations of  $\alpha$ -lath thickness, oxygen enhancement, and prior- $\beta$  particle size.<sup>(20)</sup>

**3.1.3 Atomic Force Microscope**

The two-dimensional and three-dimensional pictures obtained from the Atomic Force Microscope were used to evaluate the surface roughness of the Gyroid lattice Ti-6Al-4V surface as shown in Figure 3 a, b respectively. The vertical deviation of the 3D pictures was construed to signify surface roughness. Because of the porosity relative to the surface area where a high surface roughness was developed. The topographies of Ti alloy before wear show different features in AFM pictures. The surface’s grains are asymmetrically distributed and have a root mean square average roughness (Rq) of around 0.395  $\mu\text{m}$  and a maximum peak height of 1.71  $\mu\text{m}$ . Figure 3 c, d represent the height-distance line profiles and evenly dispersed particles, with height ranges of 0.324  $\mu\text{m}$  to 2.91  $\mu\text{m}$ .

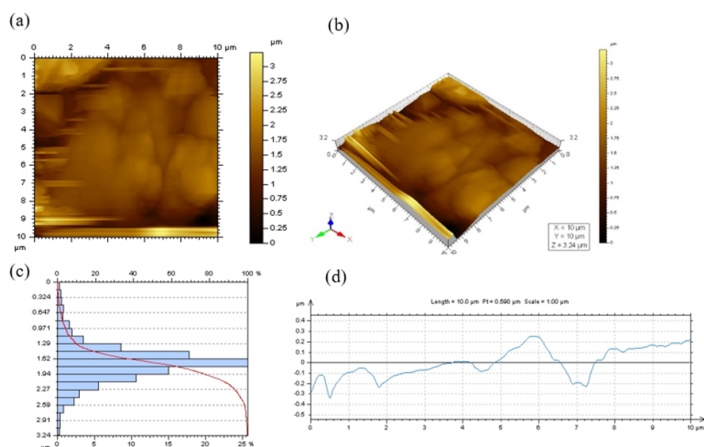


Fig 3. AFM Topography of Ti-6Al-4V samples before wear a) two- dimensional b) three- dimensional images c) Height – distance profiles d) particle distribution histogram of Ti-6Al-4V gyroid lattice structure

The surface of the as-cast Ti alloy is shown in Figure 4, it has a maximum peak height of 76.1 nm and its asymmetrically dispersed with grains that have a root mean square average roughness (Rq) of around 11.3 nm<sup>(21)</sup>.

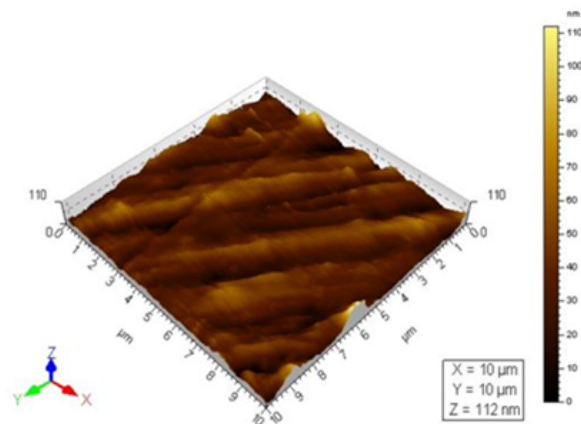


Fig 4. AFM Topography of as- cast Ti-6Al-4V three-dimensional image

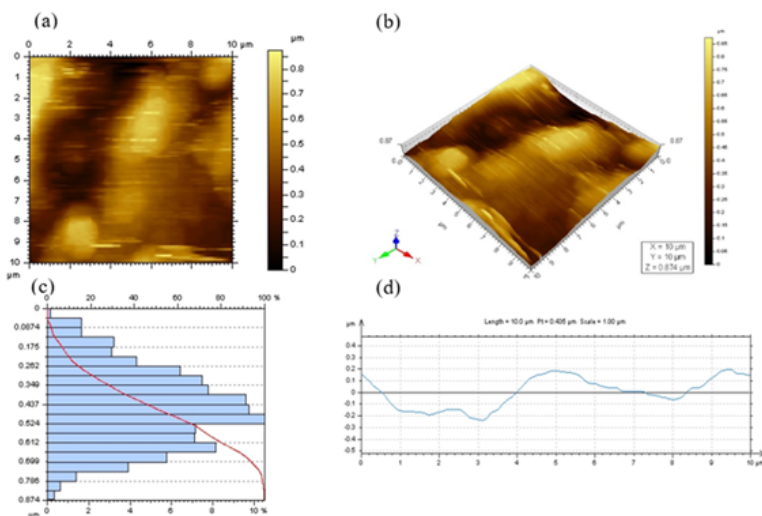


Fig 5. AFM Topography of Ti-6Al-4V samples After wear a) two-dimensional b) three- dimensional images c) Height – distance profiles d)particle distribution histogram of Ti-6Al-4V gyroid lattice structure

The vertical deviation of the 3D picture was constructed to signify the surface roughness. The worn-out samples show uniformly distributed grains without any major defects. The average roughness is found to be 0.168 μm and highest peak of roughness is stood at 0.451 μm. Figure 5 c, d represent the height-distance line profiles and evenly dispersed particles, respectively, with height ranges of 0.0874μm to 0.874μm.

### 3.1.4 X-Ray crystallography (XRD)

The XRD results of Ti-6Al-4V alloy was displayed in Figure 6.

The X-ray diffraction (XRD) analysis indicated that the alloy microstructure mostly consisted of the Ti α phase, which exhibits a hexagonal close-packed (hcp) crystal structure, along with some presence of the Ti β phase, characterised by a body-centred cubic (bcc) crystal structure. The diffraction peaks originating from the α phase are readily discernible in the pattern. The sample’s primary peaks are obtained from the α (hcp) phase. The samples showed the emergence of a peaks at 2θ = 35.460°,

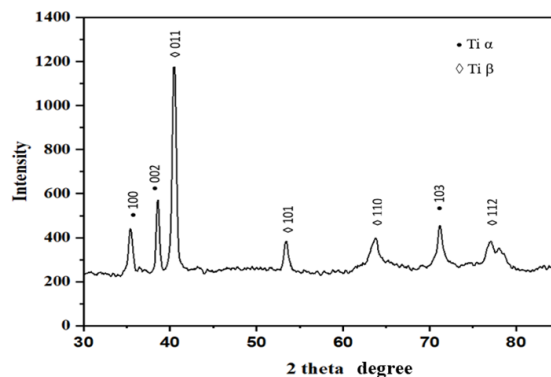


Fig 6. XRD of Ti-6Al-4V alloy

38.598°, 63.834°, 71.214° as Ti- $\alpha$  phase and confirming the presence of secondary  $\beta$  phase at the peak of  $2\theta = 40.457^\circ, 53.492^\circ, 77.021^\circ$  as Ti- $\beta$  phase respectively. Using Panalytical HighScore software, all of the peaks were indexed and compared with the diffraction data (01-089-5009) of powder Ti alloy (22). From this XRD analysis, it is evidently proved that Ti- $\alpha$  and Ti- $\beta$  phases has been evolved in the Additively manufactured Ti-6Al-4V samples.

### 3.2 Tribological Evaluation

The wear test specimen was printed according to the ASTM standard G99 (23). In this study, effect of load and sliding velocity and their influences of wear characteristics were discussed in detail.

#### 3.2.1 Effect of Load on COF and Wear rate

Figure 7 a, b displays the influence of load and sliding velocity on the COF and wear rate of Gyroid Ti alloy and as cast samples respectively.

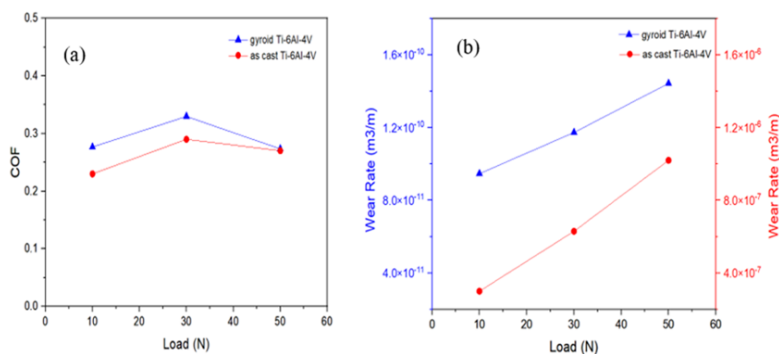


Fig 7. a, b: Effect of Load on COF and Wear rate

The 3D printed sample has a maximum coefficient of friction of 0.34 and a lowest coefficient of friction of 0.26. For the printed Gyroid lattice sample, the maximum and minimum wear values are  $1.49 \times 10^{-10} \text{ m}^3/\text{m}$  and  $0.9 \times 10^{-10} \text{ m}^3/\text{m}$ , respectively. The lowest wear rate for as cast Ti-6Al-4V substrate is  $0.39 \times 10^{-6} \text{ m}^3/\text{m}$ , while the maximum wear rate is  $1.19 \times 10^{-6} \text{ m}^3/\text{m}$ . The coefficient of friction rises with the load, till the load value is raised to 30N, however, when the load is increased to 50N, the coefficient of friction rapidly falls. Due to material deterioration on the surface, the wear rate massively elevated as the applied load increased. This may be explained by the phenomenon where, under larger loads, the melt at the contact might have served as a lubricant, greatly lowering the coefficient of friction value (24). Additionally, as the load increases, the wear keeps getting higher, which might be a result of the contact melting under hydrodynamic pressure (25). The maximum wear rate of 50N for cast Ti-6Al-4V is  $1.19 \times 10^{-6} \text{ m}^3/\text{m}$ , while the maximum wear rate of additively printed Ti-6Al-4V is  $1.49 \times 10^{-10}$  which is attributed to

its micro hardness of 460 HV.

### 3.2.2 Effect of sliding velocity on COF and Wear rate

Figure 8 a, b displays the effect of sliding velocity on the COF and wear rate of the Gyroid Ti-6Al-4V samples.

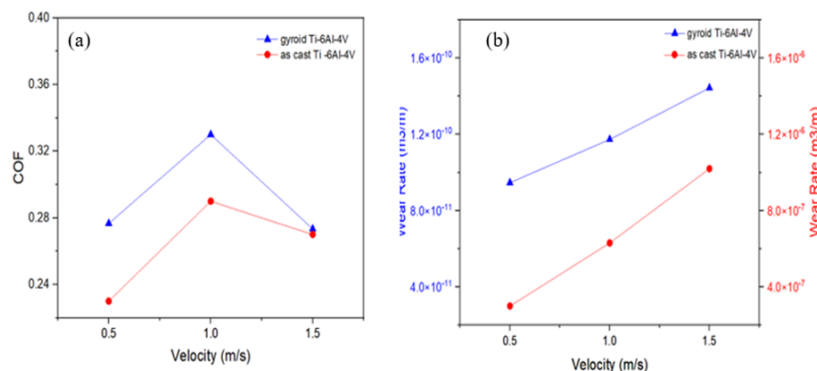


Fig 8. a, b: Effect velocity on COF and Wear rate

A higher coefficient of friction of 0.34 is obtained for the sliding velocity of 1.0 m/s. The highest wear rate is found to be  $1.49 \times 10^{-10} \text{ m}^3/\text{m}$  at 1.5 m/s for Gyroid lattice structured specimen. With an increase in velocity, both the COF and wear rate increased significantly. At higher velocities, wear debris are removed more quickly<sup>(26)</sup>, and the detached wear debris might be acted as a third body abrasive, which would greatly increase the coefficient of friction at the contact. The inadequate resistance to wear of Ti-6Al-4V is commonly ascribed to either insufficient thickness in the protective passive surface that is generated or to the occurrence of plastic deformation. The as cast Ti-6Al-4V substrate's coefficient of friction ranged from 0.23 to 0.26. Due to the ductile character and low work hardening properties of titanium alloy, the additively produced Gyroid lattice Ti-6Al-4V substrate of COF range from 0.29 to 0.31 which exhibits substantial amount of friction<sup>(27)</sup>.

### 3.3 Wear Mechanism maps of Gyroid Ti using FC mean Algorithm and PNN mapping

In order to classify the different wear modes for this study Fuzzy C- means Algorithm is adopted. The wear modes are categorized as mild wear, severe wear and ultra severe wear<sup>(28)</sup>. The wear mechanisms map of Ti-6Al-4V was constructed using the Probabilistic Neural Network tool in MATLAB software based on the following procedure<sup>(29)</sup>. The normal load is marked on the X-axis, while the sliding velocity is marked on the Y-axis and the resultant wear rate is plotted on the Z- axis. The methods involved in constructing the wear map mechanism by Probabilistic Neural Network is given as follows<sup>(30)</sup>.

- The input vectors are normal load, sliding velocity and wear rate.
- From the numerical wear map, an instance of data points spanning the complete mechanisms is gathered.
- With the help of tool lit new PNN, a dual layered network is created. A radial basis transit function neuron in the first layer uses the Euclidean interval load function to compute the output of the layer through its net input by concerning weights to the input in order to get weighted input.
- Usually, a net input result combines its weighted input and biases.
- A competitive transfer function neuron in the second layer determines the layer's outcome from its net input; by adding weighted input using a dot product weight function.
- The usual spacing between input vectors is specified by spread.
- Simulation is completed by the combined output from the two layers, based on the class it belongs. The neuron, which is an output layer generates a binary output value matching to the maximum PDF.
- Figure 9 depicts the probabilistic neural network utilised for the construction of wear mechanism of gyroid Ti-6Al-4V alloy.

Parzen estimators, provide the PDF needed by Bayes theory, are also used in the network paradigm. If the distributions from which the data originate are known, this theory describes how to construct an ideal classifier. Think of a pattern vector with X

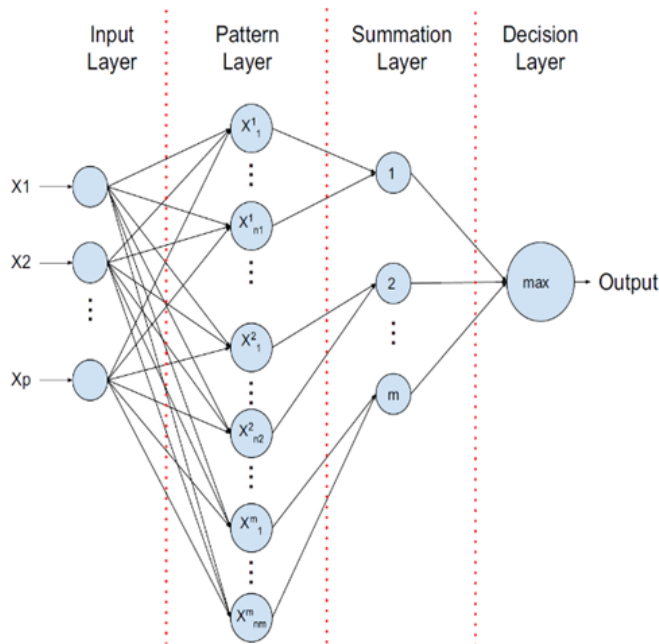


Fig 9. Architecture of PNN

and  $M$  dimensions that belongs to either  $K_1$  or  $K_2$ . Provide the PDF for categories  $K_1$  and  $K_2$  as  $F_1(X)$  and  $F_2(X)$ , respectively. According to Bayes' decision rule,  $X$  is a member of  $K_1$  if:

$$F_1(X)/F_2(X) > L_1 P_2 / L_2 P_1 \tag{1}$$

Conversely,  $X$  belongs to  $K_2$  if:

$$F_1(X)/F_2(X) < L_1 P_2 / L_2 P_1 \tag{2}$$

Where  $P_1$  is the prior probability of occurrence of category  $K_1$ ,  $P_2$  is the prior probability of occurrence of category  $K_2$ ,  $L_1$  is the loss or cost function associated with misclassifying the vector as belonging to category  $K_1$  when it belongs to category  $K_2$ , and  $L_2$  is the loss function associated with misclassifying the vector as belonging to category  $K_2$  while it belongs to category  $K_1$ . The loss functions and the prior probability can frequently be regarded as being identical. Hence, estimating the probability bulk functions from the instruction patterns is the key to applying the decision rules provided by Equations (1) and (2)<sup>(31)</sup>.

Figure 10 exhibits the wear mechanism map for Ti-6Al-4V alloys with a Gyroid lattice structure that were additively manufactured. The mild wear regime in Figure 10a demonstrates the dominance of the abrasion where a flake-like debris is produced by fractures initiated by shear<sup>(32)</sup>.

The surface-shows scratch-like deep grooves that run parallel to the path of wear were created by the abrasive particles being micro-cut. This mechanism was achieved for the test at a sliding velocity of 1.5 m/s and normal load of 10–50 N, as illustrated in Figure 10b. Due to constant sliding between the surfaces, adequate temperature is produced between them, leading to oxidation wear, as shown in the mild wear regime.

Figure 10 c shows the severe wear regime of wear mechanism map. Just a small fraction of the material that has been moved by ploughing actually separates from the surface, though the topography has been altered. Deep long cracks seen on the specimen are unchanging with surface fatigue carried over by repeated ploughing. This mechanism was achieved for the test at a sliding velocity of 1m/s and an applied force of 30–50. As material is ploughed, it deforms plastically under the load. Further applications of loads cause microcracks to grow through the distorted materials, which are finally formed by brittle fracture.

Figure 10d represents the severe wear regime, demonstrates the predominance of delamination mechanism, or the separation of material into flake- or sheet-like particles. The presence of rigid particles between the rubbing surfaces caused more surface cracks to occur, physically deforming the oxide particles on the sliding surfaces. The severe wear regime's wear values vary from  $1.1 \times 10^{-10} \text{ m}^3/\text{m}$  to  $1.49 \times 10^{-10} \text{ m}^3/\text{m}$ . Figure 10 d shows the dominance of melting wear with the wear rate higher than

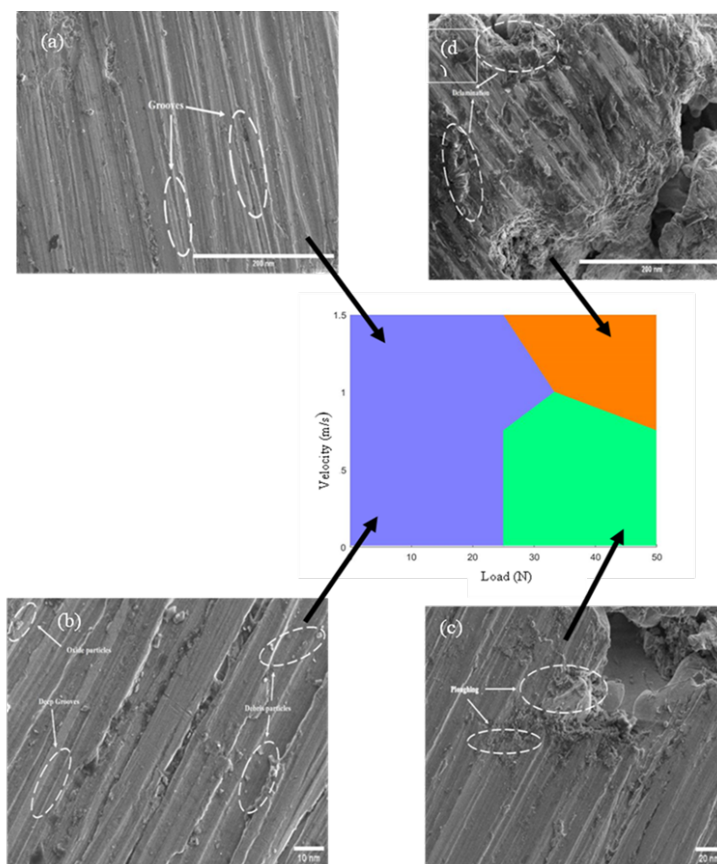


Fig 10. Wear mechanism map for printed Gyroid lattice structured Ti-6Al-4V a) Abrasion b) Oxidation c) deformation d) delamination

$1.49 \times 10^{-10} \text{ m}^3/\text{m}$  in the ultra-severe wear regime. The Melting mechanism was developed as a result of heat being created at the contacting surface interface, and which is linked to chemical reactivation. When subject to modest loads, plastic deformation and fractures initially occurred on worn surface which is attributed to the high strength quality of Ti-6Al-4V.

## 4 Conclusion

- A Gyroid lattice structure was designed using CREO and implicated for the fabrication of Gyroid Ti-6Al-4V using DMLS.
- The presence of Ti-6Al-4V alloy is confirmed through XRD studies.
- The Surface roughness of Gyroid Ti is found to be 0.395 microns before wear study and 0.168 microns after wear study.
- The Micro hardness of Gyroid Ti-6Al-4V is clocked to 460 HV as the rate of cooling is more than 525 K/s comparatively micro hardness of as cast Ti alloy is 358 HV.
- The wear resistance of Gyroid Ti-6Al-4V is far better than that of as cast Ti-6Al-4V alloys. Gyroid Ti has achieved a maximum wear rate of  $1.49 \times 10^{-10} \text{ m}^3/\text{m}$ , while the as cast Ti alloy has achieved the maximum wear rate of  $1.19 \times 10^{-6} \text{ m}^3/\text{m}$ .
- Fuzzy C-means algorithm classified the wear modes and a new PNN tool in MAT LAB drew wear map mechanism for Gyroid Ti alloy.
- The predominant wear mechanism that are identified for the wear characteristics if Ti-6Al-4V alloys are abrasion, oxidation, deformation and delamination.
- From the wear mechanism map it is observed that mild wear is influenced by abrasion and oxidation mechanism, while severe wear is dominated by deformation mechanism. Delamination mechanism is found to be predominant in ultra severe mode.
- The unique work of this study is to explore a wear mechanism mapping of Gyroid Ti-6Al-4V. This mapping is accomplished by the use of the PNN tool by the MATLAB software. Furthermore, the Fuzzy C-means algorithm has been employed to classify the different modes for the mapping.

- Scanty of literature are available in the wear mapping of as cast Ti-6Al-4V but there are no literature available for the Additively printed Ti-6Al-4V for discussing the Wear mechanisms and its wear mapping using Probabilistic Neural Network.
- Future scope is to study the various structures of Additively manufactured Ti-6Al-4V with controlled process parameters for the Tribological studies using python programming.

## References

- 1) Gadagi B, Lekurwale R. A review on advances in 3D metal printing. *Materials Today: Proceedings*. 2021;45(Part 1):277–283. Available from: <https://doi.org/10.1016/j.matpr.2020.10.436>.
- 2) Salmi M. Additive Manufacturing Processes in Medical Applications. *Materials*. 2021;14(1):1–16. Available from: <https://doi.org/10.3390/ma14010191>.
- 3) Chen LY, Liang SX, Liu Y, Zhang LC. Additive manufacturing of metallic lattice structures: Unconstrained design, accurate fabrication, fascinated performances, and challenges. *Materials Science and Engineering: R: Reports*. 2021;146:100648. Available from: <https://doi.org/10.1016/j.mser.2021.100648>.
- 4) Mondal P, Das A, Wazeer A, Karmakar A. Biomedical porous scaffold fabrication using additive manufacturing technique: Porosity, surface roughness and process parameters optimization. *International Journal of Lightweight Materials and Manufacture*. 2022;5(3):384–396. Available from: <https://doi.org/10.1016/j.ijlmm.2022.04.005>.
- 5) Liverani E, Rogati G, Pagani S, Brogini S, Fortunato A, Caravaggi P. Mechanical interaction between additive-manufactured metal lattice structures and bone in compression: implications for stress shielding of orthopaedic implants. *Journal of the Mechanical Behavior of Biomedical Materials*. 2021;121:104608. Available from: <https://doi.org/10.1016/j.jmbbm.2021.104608>.
- 6) Benady A, Meyer SJ, Golden E, Dadia S, Levy GK. Patient-specific Ti-6Al-4V lattice implants for critical-sized load-bearing bone defects reconstruction. *Materials & Design*. 2023;226:1–13. Available from: <https://doi.org/10.1016/j.matdes.2023.111605>.
- 7) Acquesta A, Monetta T. As-Built EBM and DMLS Ti-6Al-4V Parts: Topography–Corrosion Resistance Relationship in a Simulated Body Fluid. *Metals*. 2020;10(8):1–15. Available from: <https://doi.org/10.3390/met10081015>.
- 8) Azarniya A, Colera XG, Mirzaali MJ, Sovizi S, Bartolomeu F, Mare KSW, et al. Additive manufacturing of Ti-6Al-4V parts through laser metal deposition (LMD): Process, microstructure, and mechanical properties. *Journal of Alloys and Compounds*. 2019;804:163–191. Available from: <https://doi.org/10.1016/j.jallcom.2019.04.255>.
- 9) Singla AK, Banerjee M, Sharma A, Singh J, Bansal A, Gupta MK, et al. Selective laser melting of Ti6Al4V alloy: Process parameters, defects and post-treatments. *Journal of Manufacturing Processes*. 2021;64:161–187. Available from: <https://doi.org/10.1016/j.jmapro.2021.01.009>.
- 10) Koju N, Niraula S, Fotovvati B. Additively Manufactured Porous Ti6Al4V for Bone Implants: A Review. *Metals*. 2022;12(4):1–34. Available from: <https://doi.org/10.3390/met12040687>.
- 11) Sharma S, Meena A. Microstructure attributes and tool wear mechanisms during high-speed machining of Ti-6Al-4V. *Journal of Manufacturing Processes*. 2020;50:345–365. Available from: <https://doi.org/10.1016/j.jmapro.2019.12.029>.
- 12) Cai C, An Q, Ming W, Chen M. Microstructure- and cooling/lubrication environment-dependent machining responses in side milling of direct metal laser-sintered and rolled Ti6Al4V alloys. *Journal of Materials Processing Technology*. 2022;300:117418. Available from: <https://doi.org/10.1016/j.jmatprotec.2021.117418>.
- 13) Yu H, Meng X, Wang Z, Chen C. Influence of Scanning Speed on the Microstructure and Wear Resistance of Laser Alloying Coatings on Ti-6Al-4V Substrate. *Materials*. 2022;15(17):1–14. Available from: <https://doi.org/10.3390/ma15175819>.
- 14) Kelly CN, Kahra C, Maier HJ, Gall K. Processing, structure, and properties of additively manufactured titanium scaffolds with gyroid-sheet architecture. *Additive Manufacturing*. 2021;41:101916. Available from: <https://doi.org/10.1016/j.addma.2021.101916>.
- 15) Sallica-Leva E, Costa FHD, Santos CTD, Jardim AL, Silva JVL, Fogagnolo JB. Microstructure and mechanical properties of hierarchical porous parts of Ti-6Al-4V alloy obtained by powder bed fusion techniques. *Rapid Prototyping Journal*. 2022;28(4):732–746. Available from: <https://doi.org/10.1108/RPJ-04-2021-0078>.
- 16) Li J, Wu H, Liu H, Zuo D. Surface and property characterization of selective laser-melted Ti-6Al-4V alloy after laser polishing. *The International Journal of Advanced Manufacturing Technology*. 2023;128:703–714. Available from: <https://doi.org/10.1007/s00170-023-11880-6>.
- 17) Liu Y, Zhang J, Tan Q, Yin Y, Li M, Zhang MX. Mechanical performance of simple cubic architected titanium alloys fabricated via selective laser melting. *Optics & Laser Technology*. 2021;134:106649. Available from: <https://doi.org/10.1016/j.optlastec.2020.106649>.
- 18) Mahmoud D, Elbestawi MA, Yu B. Process–Structure–Property Relationships in Selective Laser Melting of Porosity Graded Gyroids. *Journal of Medical Devices*. 2019;13(3):1–11. Available from: <https://doi.org/10.1115/1.4043736>.
- 19) Thijs L, Verhaeghe F, Craeghs T, Van Humbeeck J, Kruth JP. A study of the microstructural evolution during selective laser melting of Ti-6Al-4V. *Acta Materialia*. 2010;58(9):3303–3312. Available from: <https://doi.org/10.1016/j.actamat.2010.02.004>.
- 20) Bai L, Gong C, Chen X, Sun Y, Zhang J, Cai L, et al. Additive Manufacturing of Customized Metallic Orthopedic Implants: Materials, Structures, and Surface Modifications. *Metals*. 2019;9(9):1–26. Available from: <https://doi.org/10.3390/met9091004>.
- 21) Caha I, Alves AC, Chirico C, Tsipas SA, Rodrigues IR, Pinto AMP, et al. Interactions between wear and corrosion on cast and sintered Ti-12Nb alloy in comparison with the commercial Ti-6Al-4V alloy. *Corrosion Science*. 2020;176:108925. Available from: <https://doi.org/10.1016/j.corsci.2020.108925>.
- 22) Fiolek A, Zimowski S, Kopia A, Moskalewicz T. The Influence of Electrophoretic Deposition Parameters and Heat Treatment on the Microstructure and Tribological Properties of Nanocomposite Si3N4/PEEK 708 Coatings on Titanium Alloy. *Coatings*. 2019;9(9):1–17. Available from: <https://doi.org/10.3390/coatings9090530>.
- 23) Skvortsova S, Orlov A, Valyano G, Spektor V, Mamontova N. Wear Resistance of Ti-6Al-4V Alloy Ball Heads for Use in Implants. *Journal of Functional Biomaterials*. 2021;12(4):1–10. Available from: <https://doi.org/10.3390/jfb12040065>.
- 24) Alemanno F, Peretti V, Tortora A, Spriano S. Tribological Behaviour of Ti or Ti Alloy vs. Zirconia in Presence of Artificial Saliva. *Coatings*. 2020;10(9):1–10. Available from: <https://doi.org/10.3390/coatings10090851>.
- 25) Attar H, Bermingham MJ, Ehtemam-Haghighi S, Dehghan-Manshadi A, Kent D, Dargusch MS. Evaluation of the mechanical and wear properties of titanium produced by three different additive manufacturing methods for biomedical application. *Materials Science and Engineering: A*. 2019;760:339–345. Available from: <https://doi.org/10.1016/j.msea.2019.06.024>.

- 26) Wang B, Zhao X, Li S, Huang S, Lai W, You D, et al. Self-lubricating coating with zero weight loss performance on additively manufactured Ti-6Al-4V. *Surface and Coatings Technology*. 2022;447:128847. Available from: <https://doi.org/10.1016/j.surfcoat.2022.128847>.
- 27) Williams DF. Specifications for Innovative, Enabling Biomaterials Based on the Principles of Biocompatibility Mechanisms. *Frontiers in Bioengineering and Biotechnology*. 2019;7:1–10. Available from: <https://doi.org/10.3389/fbioe.2019.00255>.
- 28) Jagadeesh GV, Setti SG. Tribological Performance Evaluation of Ball Burnished Magnesium Alloy for Bioresorbable Implant Applications. *Journal of Materials Engineering and Performance*. 2022;31(2):1170–1186. Available from: <https://doi.org/10.1007/s11665-021-06228-8>.
- 29) Özerinç S, Kaygusuz B, Kaş M, Motallebzadeh A, Nesli Ş, Duygulu Ö, et al. Micromechanical Characterization of Additively Manufactured Ti-6Al-4V Parts Produced by Electron Beam Melting. *JOM*. 2021;73(10):3021–3033. Available from: <https://doi.org/10.1007/s11837-021-04804-w>.
- 30) Jamshidi P, Aristizabal M, Kong W, Villapun V, Cox SC, Grover LM, et al. Selective Laser Melting of Ti-6Al-4V: The Impact of Post-processing on the Tensile, Fatigue and Biological Properties for Medical Implant Applications. *Materials*. 2020;13(12):1–16. Available from: <https://doi.org/10.3390/ma13122813>.
- 31) Azarniya A, Colera XG, Mirzaali MJ, Sovizi S, Bartolomeu F, Mare KSW, et al. Additive manufacturing of Ti-6Al-4V parts through laser metal deposition (LMD): Process, microstructure, and mechanical properties. *Journal of Alloys and Compounds*. 2019;804:163–191. Available from: <https://doi.org/10.1016/j.jallcom.2019.04.255>.
- 32) Wang M, Jia S, Chen E, Yang S, Liu P, Qi Z. Research and application of neural network for tread wear prediction and optimization. *Mechanical Systems and Signal Processing*. 2022;162:108070. Available from: <https://doi.org/10.1016/j.ymssp.2021.108070>.